Flight Trajectory Optimization of Fly-Gen AWE Systems through a Harmonic Balance Method

Filippo Trevisi[1], **Iván Castro-Fernández**[2], **Gregorio Pasquinelli**[1], **Carlo Emanuele Dionigi Riboldi**[1], **and Alessandro Croce**[1]

[1]Department of Aerospace Science and Technology, Politecnico di Milano, Via La Masa 34, 20156 Milano, Italy

[2]Department of Aerospace Engineering, Universidad Carlos III de Madrid, Leganés, 28911 Madrid, Spain

Correspondence: F. Trevisi (filippo.trevisi@polimi.it)

Abstract. The optimal control problem for flight trajectories of Fly-Gen Airborne Wind Energy Systems (AWES) is a crucial research topic for the field, as suboptimal paths can lead to a drastic reduction in power production. One of the novelties of the present work is the expression of the optimal control problem in the frequency domain through a Harmonic Balance formulation. This allows to potentially reduce the problem size by solving only for the main harmonics and to implicitly impose periodicity of the solution. The trajectory is described by the Fourier coefficients of the dynamics (elevation and azimuth angles) and of the control inputs (on-board wind turbines thrust and AWES roll angle). To isolate the effects of each physical phenomenon, optimal trajectories are presented with an increasing level of physical representation from the most idealized case: i) If the mean thrust power (mechanical power linked to the dynamics) is considered as the objective function, optimal trajectories are characterized by a constant AWES velocity over the loop and a circular shape. This is done by converting all the gravitational potential energy into electrical energy. At low wind speed, on-board wind turbines are then used as propellers in the ascendant part of the loop; ii) If the mean shaft power (mechanical power after momentum losses) is the objective function, a part of the potential energy is converted into kinetic and the rest into electrical energy. Therefore, the AWES velocity fluctuates over the loop; iii) If the mean electrical power is considered as the objective function, the on-board wind turbines are never used as propellers because of the power conversion efficiency. Optimal trajectories for case ii) and iii) have a circular shape squashed along the vertical direction. The optimal control inputs can be generally modelled with one harmonic for the on-board wind turbines thrust and two for AWES roll angle without a significant loss of power, demonstrating that the absence of high-frequency control is not detrimental to the power generated by Fly-Gen AWES.

1 Introduction

Airborne Wind Energy (AWE) is the branch of wind energy which aims at harvesting energy from the wind using airborne systems. Airborne Wind Energy Systems can be classified according to the flight operations, which are linked to the power generation technique. The flight operations can be divided into crosswind, tether-aligned and rotational, as discussed by Vermillion et al. (2021). Electrical power can be generated by a fixed or a moving ground station or, alternatively, it can be directly generated on-board and transmitted to the ground through the tether. The wing type, soft or fixed, additionally classifies the AWES. This paper focuses on AWES based on a fixed-wing with on-board generation, known as Fly-Gen AWES. However, the methods developed can be applied to other AWE architectures, after an appropriate rework of the dynamic models. These methods are suitable for investigating the optimal trajectories of AWES and, especially when applied to low fidelity models, for understanding their physical characteristics. The interpretation of the physical characteristics of optimal trajectories and the analysis of how they are influenced by parameters describing the system and its operation is the main goal of this work. With this aim, solutions are compared with analytical results coming from first-principle models whenever possible.

The first analytical power equation of crosswind AWES was derived by Loyd (1980), and additional refinements, such as the one proposed by Trevisi et al. (2020a), made an effort to modify analytic equations to include gravitational and centrifugal effects. This kind of analytical models can be used to study how power and other relevant trends approximately scale with design parameters. However, they typically neglect the system dynamics and its effect on power generation. These effects can be studied with dynamical models, ranging from low to high fidelity. Typically, low- to mid-fidelity models are used to investigate optimal trajectories of AWE. Low-fidelity dynamic models are characterized by multiple assumptions, which simplify the models, and by the low computational cost. The quasi-steady model (van der Vlugt et al. (2019)) assumes the kite as a point mass in steady state for each point of the loop. This model is validated with experimental data (Schelbergen and Schmehl (2020)) and it is considered accurate for soft kites, where the inertia is low and the AWES quickly reaches the steady state. A similar approach is considered while deriving the Unicycle model (Fagiano et al. (2014); Vermillion et al. (2021)). Also this model, based on a point mass, is developed for soft-wing AWES and computes the velocity vector via quasi-steady flight equations. The kite orientation is found by a turning law that is derived from lateral force equilibrium and is validated through a number of experiments. The Unifoil model (Cobb et al. (2020)) is derived by modification of the Unicycle model in order to be applied to fixed-wing AWES. Indeed, the quasi-steady assumption is removed and the turning maneuvers modelled with a yaw dynamic equation.

Higher fidelity, but still computationally efficient, dynamic models are developed by Sánchez-Arriaga et al. (2017, 2019) and Sánchez-Arriaga and Serrano-Iglesias (2021) as a part of the Lagrangian Kite Flight Simulators (LAKSA) package based on minimal coordinates, and by Gros and Diehl (2013) to study the dynamics of multiple AWES configurations. Moreover, thorough Newtonian dynamic models are used to compute reference flight paths and the consequent flight path control for soft-wing AWES (Fechner et al. (2015); Fechner and Schmehl (2016)) and for fixed-wing AWES (Licitra et al. (2019); Malz et al. (2019); Eijkelhof and Schmehl (2022)).

The dynamic models just introduced are particularly suitable to be used within optimal control studies for their computational inexpensiveness and for the reduced number of nonlinearities compared to even higher fidelity codes, such as kiteFAST (Jonkman et al. (2018)). The Unicycle and Unifoil models, introduced earlier, are mainly used to compute reference flight paths and for flight path control development (Cobb et al. (2020); Fernandes et al. (2021)). To ease the deployment of optimal control problems for AWE, *awebox* (awebox (2022)) is developed and used, for instance by Leuthold et al. (2018), Haas et al. (2019) and De Schutter et al. (2019), to solve optimal control problems. *awebox* solves optimal control problems in time, imposing periodicity constraints. A similar optimal control problem is studied

by Horn et al. (2013), Malz et al. (2020a) and Malz et al. (2020b), where the optimal trajectory is found in time using a discretization by direct collocation and a homotopy strategy based on the relaxation of the dynamic constraints (Gros et al. (2013)). Licitra et al. (2019) solved an optimal control problem with an experimentally validated dynamic model of a Ground-Gen AWES. They find that, under some prescribed constraints, circular and figure of eight trajectories produce similar mean power and that closed-loop control enhance robustness but decreases power production of about 10 %. Control in all operation phases is studied by Rapp et al. (2019) and Todeschini et al. (2021): the present work can be understood as a study of the guidance (or the reference trajectory) used during the power generation phase of their study.

Pasquinelli (2021) investigates the power losses in a circular trajectory with a dynamical quasi-analytical model. He finds that the causes of power losses are mainly two: the AWES span non-perpendicularity with respect to the incoming wind during the motion and the AWES speed fluctuation over the loop. Makani team (Tucker (2020)) studies the flight trajectories of Fly-Gen AWES with a simplified quasi-analytical approach, aiming at describing their physical characteristics. They run their flight simulator for different trajectories and production strategies to derive analytical expressions, which can describe the consequences of different operational choices. Their production strategy at low wind speed is to convert part of the potential energy into kinetic and part into electrical, when the AWES moves downward. To reduce the potential energy exchange, they suggest to squash the trajectories along the vertical direction. Moreover, they explain that using electrical power to push the AWES upward drastically decreases the overall power production, as power needs to be converted from mechanical to electrical and again from electrical to mechanical, so that the related efficiencies are counted twice. They, in accord with the study for Ground-Gen by Stuyts et al. (2015), conclude that the electrical conversion losses should be considered when deciding on the production strategy. Following these conclusions, the present work also investigates the influence of the power generation efficiencies on the optimal trajectories.

As the aim of this work is to interpret optimal trajectories in a physical way, a low-fidelity dynamic model, similar to the one proposed by Fernandes et al. (2021) (reformulated for Fly-Gen AWES), is selected. Instead of solving the dynamics and the optimal control problem in time, the present approach models the problem in the frequency domain, making use of a Harmonic Balance method, which expands the periodic solution as a Fourier series (Lau et al. (1982); Pierre and Dowell (1985); Dimitriadis (2017)). Working with the Fourier coefficients and not with the time series themselves allows to potentially reduce the problem size depending on the problem at hand, to look for periodic solutions implicitly and to study the solution in an intuitive way by looking at the contribution of the different harmonics. To the best of the authors' knowledge, this is the first work on AWES where

an optimal control problem aided by a Harmonic Balance methodology is formulated.

Even though the frequency-domain formulation can be used for any periodic flight trajectories (i.e. circular and figure of eight), only circular trajectories are here analyzed to limit the paper scope and length. Figure of eight trajectories are intended to be analyzed and intensively compared with circular trajectories in a future work.

The paper is organized as follows: in Sect. 2 the flight dynamic model, the Harmonic Balance and the optimal control statement are introduced. In Sect. 3, the main results from steady state analytical models are recalled from literature, together with the introduction of some key non-dimensional numbers used later in the analyses. In Sect. 4, the solution obtained with the Harmonic Balance formulation is validated against the time integration. In Sect. 5, optimal control problems with constant wind inflow and no constraints on the mean elevation angle is analyzed. This extreme idealization allows to understand some optimal trajectory characteristics which are also present in more realistic cases. Section 6 focuses on the results of a more realistic optimal control problem where the wind shear and a constraint on the minimum elevation angle are included in the analyses. Finally, in Sect. 7 the results are discussed and the main conclusions summarized.

2 Methodology

2.1 Flight Dynamic Model

Two coordinate systems (Figure 1a) are defined to derive the equations of motion. The ground coordinate system (denoted by $\mathcal{F}_G$) is inertial and centered at the ground station: $\mathbf{e}_x$ points downwind, $\mathbf{e}_z$ toward the Zenith and $\mathbf{e}_y$ completes the right-handed frame. For convenience, spherical coordinates are used to describe the position of the airborne unit with L_t the tether length, ϕ the azimuth angle and β the elevation angle. The spherical reference frame (denoted by $\mathcal{F}_S$) is unequivocally defined at every position with the origin at the AWES center of mass, $\mathbf{e}_r$ pointing outward the sphere in the radial direction, $\mathbf{e}_\phi$ normal to $\mathbf{e}_r$ and contained on a plane parallel to $x - y$ and $\mathbf{e}_\beta = \mathbf{e}_r \times \mathbf{e}_\phi$. The position $\mathbf{p}$, velocity $\mathbf{v}$ and acceleration $\mathbf{a}$ vectors projected into the spherical reference frame $\mathcal{F}_S$ are

$$
\begin{aligned}
\mathbf{p} &= L_t \mathbf{e}_r, \\
\mathbf{v} &= L_t \dot{\phi} \cos \beta \mathbf{e}_\phi + L_t \dot{\beta} \mathbf{e}_\beta, \\
\mathbf{a} &= \left(-L_t \dot{\phi}^2 \cos^2 \beta - L_t \dot{\beta}^2 \right) \mathbf{e}_r \\
&\quad + (L_t \ddot{\phi} \cos \beta - 2 L_t \dot{\phi} \dot{\beta} \sin \beta) \mathbf{e}_\phi \\
&\quad + \left(L_t \dot{\beta}^2 \sin \beta \cos \beta + L_t \ddot{\beta} \right) \mathbf{e}_\beta.
\end{aligned}
\tag{1}
$$

The wind velocity is in the positive x-axis direction of $\mathcal{F}_G$ and projected into the spherical reference frame is

$$
\begin{aligned}
\mathbf{v}_w &= v_w \left(\cos \phi \cos \beta \mathbf{e}_r - \sin \phi \mathbf{e}_\phi - \cos \phi \sin \beta \mathbf{e}_\beta \right), \\
v_w(h) &= v_{w,0} \left(\frac{h}{h_0} \right)^{\alpha_s} = v_{w,0} \left(\frac{L_t}{h_0} \sin \beta \right)^{\alpha_s},
\end{aligned}
\tag{2}
$$

where the wind speed v_w as function of the altitude h is modelled with an exponential law: $v_{w,0}$ is the reference wind speed at the reference altitude h_0 and α_s is the wind shear exponent. The relative speed between the AWES and the wind is

$$
\mathbf{v}_r = \mathbf{v}_w - \mathbf{v}.
\tag{3}
$$

To describe the AWES attitude, a non sideslip velocity constraint is included in the modelling. Indeed, the wing operates at the highest performance under this condition. To impose this constraint implicitly, the unit vector $\mathbf{e}_1$ is defined to point to the direction opposite to the relative wind speed

$$
\mathbf{e}_1 = -\frac{\mathbf{v}_r}{|\mathbf{v}_r|}.
\tag{4}
$$

The spanwise unit vector $\mathbf{s}$ (with origin at the center of mass and pointing in the right-wing span direction) is defined perpendicular to $\mathbf{e}_1$ with the procedure illustrated in Fig. 1b. A second vector $\mathbf{e}_3$ is defined as a unit vector in a plane parallel to the $x - z$ plane with elevation β_s (and negative sign)

$$
\begin{aligned}
\mathbf{e}_3 &= -(\mathbf{e}_x \cos(\beta_s) + \mathbf{e}_z \sin(\beta_s)), \\
\mathbf{e}_x &= \cos \phi \cos \beta \mathbf{e}_r - \sin \phi \mathbf{e}_\phi - \cos \phi \sin \beta \mathbf{e}_\beta, \\
\mathbf{e}_z &= \sin \beta \mathbf{e}_r + \cos \beta \mathbf{e}_\beta.
\end{aligned}
\tag{5}
$$

Note that $\mathbf{e}_3$ points upwind when $\beta_s = 0$. The unit vector $\mathbf{e}_2$ is then defined as

$$
\mathbf{e}_2 = \frac{\mathbf{e}_3 \times \mathbf{e}_1}{|\mathbf{e}_3 \times \mathbf{e}_1|},
\tag{6}
$$

where $|\mathbf{e}_3 \times \mathbf{e}_1|$ can take values smaller than one because $\mathbf{e}_3$ and $\mathbf{e}_1$ are not defined to be perpendicular in general. In this way, $\mathbf{e}_2$ is perpendicular to the plane $\mathbf{e}_3$-$\mathbf{e}_1$. Rodrigues' formula is then used to define $\mathbf{s}$ through a rotation of ψ around $\mathbf{e}_1$, starting from $\mathbf{e}_2$

$$
\mathbf{s} = \mathbf{e}_2 \cos \psi + (\mathbf{e}_1 \times \mathbf{e}_2) \sin \psi + \mathbf{e}_1 (\mathbf{e}_1 \cdot \mathbf{e}_2)(1 - \cos \psi).
\tag{7}
$$

With this formulation, $\mathbf{s}$ is defined to be always perpendicular to the relative wind and its components are defined by a unique angle ψ, called hereafter roll angle. When $\psi = 0$, $\mathbf{s}$ is perpendicular to $\mathbf{e}_3$.

The aerodynamic lift $\mathbf{L}$ and the drag $\mathbf{D}$ take the standard form

$$
\mathbf{L} = \frac{1}{2} \rho A C_L |\mathbf{v}_r| \mathbf{v}_r \times \mathbf{s}, \qquad \mathbf{D} = \frac{1}{2} \rho A C_D |\mathbf{v}_r| \mathbf{v}_r,
\tag{8}
$$
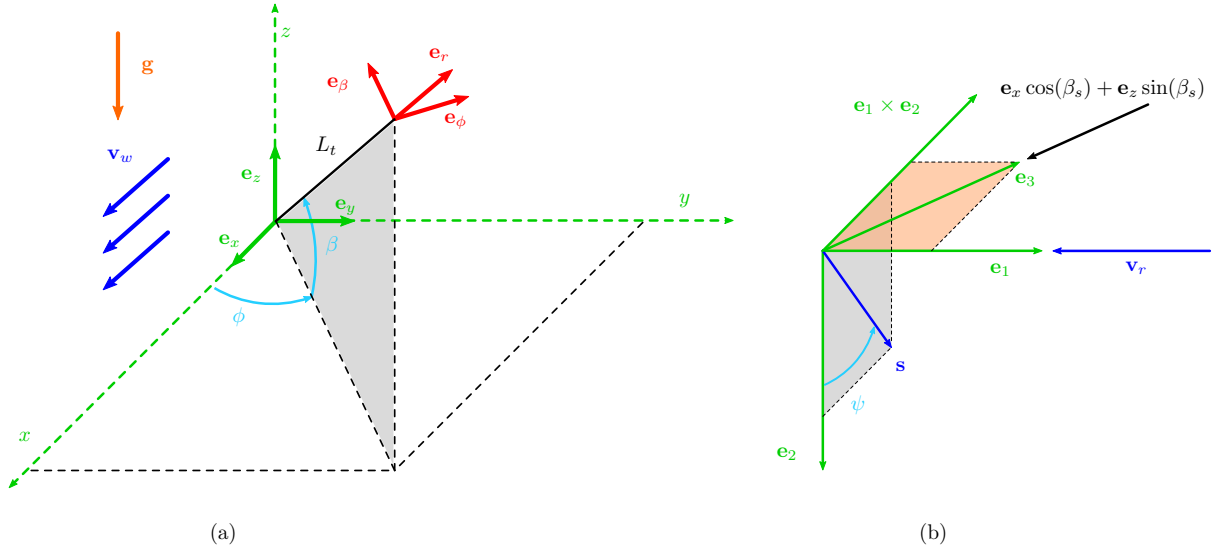
Figure 1. **(a)** Ground reference frame $\mathcal{F}_G$ ($\mathbf{e}_x - \mathbf{e}_y - \mathbf{e}_z$) and spherical reference frame $\mathcal{F}_S$ ($\mathbf{e}_r - \mathbf{e}_\phi - \mathbf{e}_\beta$) and **(b)** sketch for the spanwise unit vector $\mathbf{s}$ definition.

where ρ is the air density, A is the wing area and the lift and drag coefficients C_L and C_D are considered constant. The drag coefficient C_D includes the contribution from the tether drag (Trevisi et al. (2020a)). The gravitational force $\mathbf{F}_g$ and the tether force $\mathbf{T}$ are

$$\mathbf{F}_g = -mg(\sin\beta\mathbf{e}_r + \cos\beta\mathbf{e}_\beta), \qquad \mathbf{T} = -T\mathbf{e}_r, \qquad (9)$$

where m is the AWES mass, g the gravitational acceleration and T the norm of the tether force. The thrust produced by the on-board wind turbines $\mathbf{D}_t$ is expressed as a linear function of the aerodynamic drag with gain γ

$$\mathbf{D}_t = \gamma\mathbf{D}. \qquad (10)$$

The dynamic equations of motion in compact form read

$$m\mathbf{a} = \mathbf{L} + \mathbf{D} + \mathbf{D}_t + \mathbf{F_g} + \mathbf{T}, \qquad (11)$$

recalling that $\mathbf{a}$ is given by Eq. 1.

As the objectives of the optimal control problems are linked to the power production, three different power quantities are defined. The thrust power P_t (i.e. the power linked to the AWES dynamics) is estimated as a dot product of $\mathbf{D}_t$ and the relative velocity

$$P_t = \mathbf{D}_t \cdot \mathbf{v}_r. \qquad (12)$$

The shaft power P_s (i.e. the mechanical power that can be converted to electrical power) is modelled using 1D momentum theory (actuator disc) as

$$P_s = (1-a)P_t = \left(\frac{1}{2} + \frac{1}{2}\sqrt{1 - \gamma C_D \frac{A}{A_t}}\right)P_t, \qquad (13)$$

where the induction a is found by setting the thrust given by momentum theory ($\mathbf{T}_d = \frac{1}{2}\rho A_t(4a(1-a))|\mathbf{v}_r|\mathbf{v}_r$) equal to $\mathbf{D}_t$, as in Trevisi et al. (2020b), and A_t is the total turbine area.

Finally, the electrical power exchanged with the grid P takes into account the generator and transmission efficiency η_{el}

$$P = \begin{cases} P_s - (1-\eta_{el})P_s & \text{for } \gamma \geq 0 \\ P_s + (1-\eta_{el})P_s & \text{for } \gamma < 0. \end{cases} \qquad (14)$$

When power is generated ($\gamma > 0$), the electrical power distributed to the grid P is lower than the shaft power P_s because of electrical efficiencies. When power from the grid is used, the electrical power requested to the grid P is instead higher in absolute value compared to the shaft power P_s. To model the discontinuity in a continuous optimization framework, the logistic function is used

$$P = P_s - \left(\frac{1 - e^{-f\gamma}}{1 + e^{-f\gamma}}\right)(1-\eta_{el})P_s, \qquad (15)$$

where f is taken equal to 100.

2.2 Frequency Domain Formulation

Frequency domain formulations may present clear advantages when solving for periodic solutions of dynamic and control problems. They have the capability of solving for both stable and unstable branches of periodic solutions in an efficient way. Moreover, they potentially use less variables to describe the same problems. Since the problem of optimal trajectories for AWES has a periodic nature, the flight dynamic model just introduced is expressed in the frequency domain. The Harmonic Balance methodology is then

used to transform the differential equations of motion into a set of nonlinear algebraic equations (Dimitriadis (2017)). The equations of motion (Eq. 11) can be written as a set of second-order nonlinear differential equations in the form

$$\mathbf{f}(\mathbf{x}, \dot{\mathbf{x}}, \ddot{\mathbf{x}}, \mathbf{u}) = \mathbf{0},$$

$$\mathbf{x} = \left[\beta(t),\ \phi(t)\right]^T, \qquad \mathbf{u} = \left[\psi(t),\ \gamma(t)\right]^T, \tag{16}$$

where $\mathbf{x}$ is the state vector and $\mathbf{u}$ is the control vector. By assuming that Eq. 16 accepts periodic solutions, every variable of the state vector is expanded as a Fourier series of order N_x

$$x(t) \approx \frac{X_0}{2} + \sum_{k=1}^{N_x} X_{k,s} \sin(k\omega t) + X_{k,c} \cos(k\omega t),$$

$$\mathbf{X} = \left[X_0,\ X_{1,s},\ X_{2,s},\ ...X_{1,c},\ X_{2,c},\ ...\right]^T, \tag{17}$$

with $\omega = \dfrac{2\pi}{\mathcal{T}}$ being the fundamental frequency of the motion and $\mathcal{T}$ the period. Alternatively, the state vector can be expressed as

$$x(t) \approx \frac{A_0}{2} + \sum_{k=1}^{N_x} A_k \cos(k\omega t - \theta_k),$$

$$\mathbf{A} = \left[A_0,\ A_1,\ ...\right]^T, \quad \theta = \left[\theta_1,\ \theta_2,\ ...\right]^T, \tag{18}$$

where

$$A_0 = X_0, \quad A_k = \sqrt{X_{k,s}^2 + X_{k,c}^2}, \quad \theta_k = \arctan\left(\frac{X_{k,s}}{X_{k,c}}\right). \tag{19}$$

The first and second time derivatives of the state vector can be found analytically

$$\dot{x}(t) \approx \sum_{k=1}^{N_x} k\omega \left(X_{k,s} \cos(k\omega t) - X_{k,c} \sin(k\omega t)\right),$$

$$\ddot{x}(t) \approx -\sum_{k=1}^{N_x} (k\omega)^2 \left(X_{k,s} \sin(k\omega t) + X_{k,c} \cos(k\omega t)\right). \tag{20}$$

Similarly, the control inputs, assumed to be periodic, can also be expressed as a Fourier series of order N_u

$$u(t) \approx \frac{U_0}{2} + \sum_{k=1}^{N_u} U_{k,s} \sin(k\omega t) + U_{k,c} \cos(k\omega t),$$

$$\mathbf{U} = \left[U_0,\ U_{1,s},\ U_{2,s},\ ...U_{1,c},\ U_{2,c},\ ...\right]^T, \tag{21}$$

where $N_u < N_x$ because the equations of motion need to be solved at frequencies higher than the control inputs order. By introducing Eqs. 17, 20 and 21 into Eq. 16, the equations of motion can be expanded as a Fourier series of order N_x

$$\mathbf{f}(\mathbf{X}_\beta, \mathbf{X}_\phi, \mathbf{U}_\psi, \mathbf{U}_\gamma, \omega, t) \approx$$

$$\frac{\mathbf{F}_0}{2} + \sum_{k=1}^{N_x} \mathbf{F}_{k,s} \sin(k\omega t) + \mathbf{F}_{k,c} \cos(k\omega t) = \mathbf{0}. \tag{22}$$

The Fourier coefficients of the equations of motion are found numerically by applying the Fourier coefficient definition to the time series, which should have a minimum size of $2N_x + 1$. A Galerking methodology is then applied by pre-multiplying Eq. 22 by 1, $\sin(k\omega t)$, $\cos(k\omega t)$ and subsequently integrating the resulting equation over one period. The result is a set of $2 \times (2N_x + 1)$ nonlinear algebraic equations as a consequence of the orthogonality properties of the selected basis of trigonometric functions

$$\mathbf{F} = \left[\mathbf{F}_0,\ \mathbf{F}_{1,s},\ \mathbf{F}_{2,s},\ ...\mathbf{F}_{1,c},\ \mathbf{F}_{2,c},\ ...\right]^T = \mathbf{0}, \tag{23}$$

which can be understood as the residuals of the equations of motion expressed in the frequency domain. For given periodic control inputs and a given fundamental frequency, the periodic solution can be found by looking for the Fourier coefficients $[\mathbf{X}_\beta; \mathbf{X}_\phi]$ of the dynamics which solve Eq. 23.

2.3 Optimal Control Problem (OCP)

In this work, the frequency-domain formulation is included within an optimal control problem (OCP). A generic optimization problem can be written as

$$\begin{aligned} \mathcal{X}^* &= \arg\left(\min_{\mathcal{X}} obj(\mathcal{X})\right), \\ \text{s.t.:} \quad & \mathbf{lb} \leq \mathcal{X} \leq \mathbf{ub} \\ & \mathbf{g}(\mathcal{X}) \leq 0 \\ & \mathbf{h}(\mathcal{X}) = 0, \end{aligned} \tag{24}$$

where $\mathcal{X}$ are the unknown optimization variables, $\mathcal{X}^*$ their optimal values, obj the objective function, $\mathbf{lb}$ and $\mathbf{ub}$ the lower and upper bounds of $\mathcal{X}$, $\mathbf{g}$ the inequality and $\mathbf{h}$ the equality constraints. In the present formulation, the optimization variables are the Fourier coefficients of the state variables, of the control inputs and the fundamental frequency

$$\mathcal{X} = [\mathbf{X}_\beta; \mathbf{X}_\phi; \mathbf{U}_\psi; \mathbf{U}_\gamma; \omega]. \tag{25}$$

The negative value of the mean thrust power $\hat{P}_t$ (Eq. 12), shaft power $\hat{P}_s$ (Eq. 13) or electric power $\hat{P}$ (Eq. 15) over the loop is taken as objective function, where the symbol $\hat{\ }$ stands for the mean value over the loop. The equality constraints are the aggregation of the residuals of the equation of motion in the frequency domain $\mathbf{F}$ (Eq. 23) and additional physical constraints $\mathbf{R}$ in the frequency domain (e.g. certain quantities can be imposed to be constant over the loop)

$$\mathbf{h}(\mathcal{X}) = [\mathbf{F}(\mathcal{X}); \mathbf{R}(\mathcal{X})] = \mathbf{0}. \tag{26}$$

Inequality constraints $\mathbf{g}$, expressed in the time domain, can also be included in the problem (e.g. the minimum elevation angle over the loop can be bounded). A graphical representation of the OCP setup is given in Figure 2. The derivatives of flight dynamic model with respect to the optimization variables can be taken analytically and provided to the solver,
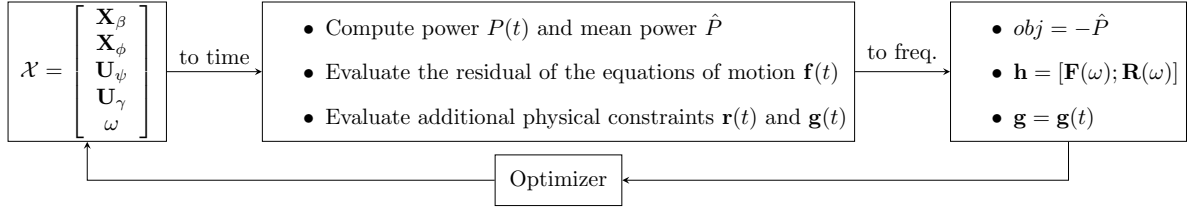
Figure 2. Graphical representation of the optimal control problem setup.

allowing for a deep and fast convergence of the solution. The OCP is implemented in *MATLAB®* environment and solved with the interior-point algorithm implemented in *fmincon*. As the chosen optimization algorithm (gradient-based) can only look for local optima, the initial guess may influence the solution. In this work, the initial guesses are taken to be circular trajectories, leading to circular shaped optimal trajectories. Figure of eight trajectories can be implemented as initial guesses, which may lead to figure of eight shaped optimal trajectories. A detailed comparison between these two trajectory types is left for future works. The OCPs are solved on an Intel Core i7-9700 3.0 Ghz, 16GB RAM. The computation times of the presented examples require from a few seconds to tens of seconds. For example, OCP A in Section 6 takes approximately 25 s, OCP B approximately 12 s.

3   Steady State Model

To compare the results of the optimal control problem with idealized analytical expressions, the main results from a refined version of the Loyd power equation (Loyd (1980)) are here briefly recalled. The thrust power equation, with the assumption of linear crosswind motion (Trevisi et al. (2020b)) is

$$
\begin{aligned}
P_{t,L} &= \frac{1}{2}\rho\, A\, v_w^3\, \gamma\, \frac{C_L}{G}\left(1+\left(\frac{G}{1+\gamma}\right)^2\right)^{3/2} \\
&= \frac{1}{2}\rho\, A\, v_w^3\, \gamma\, \frac{C_L}{G}\left(1+G_t^2\right)^{3/2},
\end{aligned}
\tag{27}
$$

where the system glide ratio (including tether drag) is $G = \frac{C_L}{C_D}$ and, for readability, a modified glide ratio is defined as $G_t = \frac{C_L}{C_D(1+\gamma)}$ by including the drag of the on-board propellers. The shaft power takes into account the on-board wind turbine induction a

$$
P_{s,L} = (1-a)P_{t,L} = \left(\frac{1}{2}+\frac{1}{2}\sqrt{1-\gamma C_D \frac{A}{A_t}}\right)P_{t,L}.
\tag{28}
$$

Finally, the power generated and sent to the grid takes into account the efficiencies of the electrical conversion

$$
P_L = \eta_{el} P_{s,L}.
\tag{29}
$$
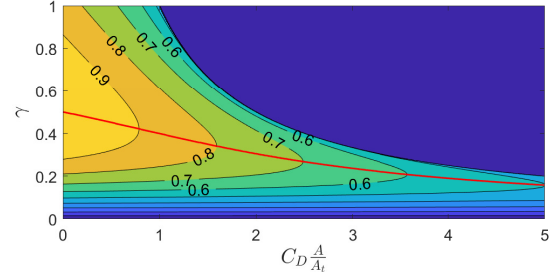
Figure 3. Normalized power $\frac{P_L}{P_L(C_D\frac{A}{A_t}=0)}$ as a function of $C_D\frac{A}{A_t}$ for high glide ratios G.

For high G, the power equation simplifies to

$$
P_L \approx \frac{1}{2}\rho\, A\, v_w^3\, C_L\, G^2\, \eta_{el}\left(\frac{1}{2}+\frac{1}{2}\sqrt{1-\gamma C_D \frac{A}{A_t}}\right)\frac{\gamma}{(1+\gamma)^3}.
\tag{30}
$$

For this expression, the value of γ which maximizes the power is only a function of the non-dimensional quantity $C_D\frac{A}{A_t}$. In Figure 3, the electrical power P_L, normalized with the maximum electrical power at $C_D\frac{A}{A_t}=0$, is plotted as a function of γ and $C_D\frac{A}{A_t}$. For increasing values of $C_D\frac{A}{A_t}$, the values of γ which maximizes power production decreases. The maximum normalized power as a function of $C_D\frac{A}{A_t}$ is shown in Fig. 4, highlighting that the analytical expression predicts a decrease in power production for increasing $C_D\frac{A}{A_t}$.

The tether force can be evaluated as

$$
T_L = \frac{1}{2}\rho\, A\, v_w^2\, \frac{C_L}{G_t}\left(1+G_t^2\right)^{3/2}.
\tag{31}
$$

Trevisi et al. (2020a) showed that for high G, neglecting gravity and with constant incoming wind, it exists an opening angle $\tilde{\Phi}$ (angle swept by the AWES during the circular trajectory, see Fig. 5) which erases the power losses due to centrifugal forces and that it is only a function of the non-dimensional mass parameter

$$
M = \frac{m}{\frac{1}{2}\rho A C_L L_t}.
\tag{32}
$$

Table 1. Reference values for the examples (Values from the Makani *MX2* description Tucker (2020)), associated non-dimensional parameters and quantities evaluated with the steady state model for γ maximizing Eq. 29.

m	2000 kg	A	54 m^2	A_t	35 m^2	L_t	300 m	C_L	1.8	C_D	0.15
η_{el}	0.8	ρ	1.225 kg m^{-3}	g	9.81 m s^{-2}	v_w	6 m s^{-1}				
G	12	M	0.1120	$C_D \frac{A}{A_t}$	0.231	γ	0.488	a	0.029	G_t	8.06
F_r	0.1106	G_r	0.1408	P_L	218.0 kW	T_L	142.6 kN	v_L	48.4 m s^{-1}	$\mathcal{T}_L$	12.6 s
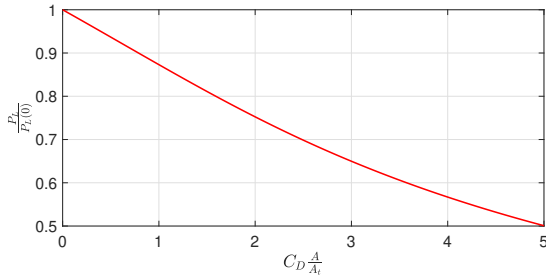
Figure 4. Maximum normalized power $\frac{P_L}{P_L(C_D \frac{A}{A_t}=0)}$ as a function of $C_D \frac{A}{A_t}$ for high glide ratios G.

In this idealized case, the turning radius is $R = L_t \sin \tilde{\Phi}$ and the revolution period is

$$\mathcal{T}_L = \frac{2\pi R}{v_L} = \frac{2\pi R}{v_w G_t}, \qquad (33)$$

where v_L is norm of the AWES velocity.

In addition to the non-dimensional mass parameter, the Froude number, which weights the fluid inertial forces to gravity forces, is used in this work

$$F_r = \sqrt{\frac{v_w^2}{g \cdot L_t}}, \qquad (34)$$

where the reference velocity is the wind velocity and the reference length is the tether length. By combining the previously introduced non-dimensional parameters, the gravity ratio G_r is defined as

$$G_r = \frac{M}{F_r^2 G_t^2} = \frac{mg}{\frac{1}{2}\rho A C_L v_w^2 G_t^2}, \qquad (35)$$

which represents the ratio between gravitational force and aerodynamic lift, similarly to the one introduced in Pasquinelli (2021).

In the following sections, the results will be generalized as a function of the non-dimensional parameters just introduced. Input parameters from Makani *MX2* design (Tucker (2020)) will be used as reference values to present the results (Table 1).

4 Validation of the Frequency-Domain Formulation against Time Integration

To make sure the frequency-domain formulation is well implemented and finds solutions which respect the equations of motion, they are compared with the solution coming from a time integration scheme. The model described in Sect. 2.1 is solved with the *MATLAB® ode45* integration scheme. After solving the periodic solution with the Harmonic Balance methodology, the Fourier coefficients of the state and control vector are retrieved. The state vector at $t = 0$ is used as an initial condition for the numerical integration. The control inputs must be computed from their Fourier series at every step of the integration. In Appendix A, a comparison for a circular and a figure of eight trajectory is shown. The solution of the dynamics, represented by the azimuth and elevation, for the two cases is equivalent demonstrating that the frequency-domain formulation is accurate enough to be used in the present optimal control problem framework.

5 Optimal Control Problems with Constant Inflow and no Elevation Angle Constraints

As the analysis is limited to circular trajectories, a cylindrical reference frame $\mathcal{F}_C$, similar to the one employed in Trevisi et al. (2020a), Trevisi et al. (2021) and Pasquinelli (2021), is used to present the results. A graphical representation of $\mathcal{F}_C$ is given in Figure 5. The longitudinal axis of $\mathcal{F}_C$ is aligned with the mean elevation angle $\hat{\beta}$. The angle β_m denotes the minimum elevation angle and Φ the opening angle. The angular position of the AWES is defined by α and when $\alpha = 0$ the AWES moves upward (i.e. $\dot{\alpha} > 0$).

To increase complexity incrementally, the optimal control problems (OCPs) are modified from the most idealized case to a realistic one. For the idealized cases analyzed in this section, uniform incoming wind speed ($\alpha_s = 0$) and no minimum elevation angle constraints are considered. In this section, β_s (Eq. 5) is set equal to zero, such that $\mathbf{e}_3$ points upwind. In this way, when the roll is equal to zero ($\psi = 0°$), the span direction is perpendicular to the incoming wind.
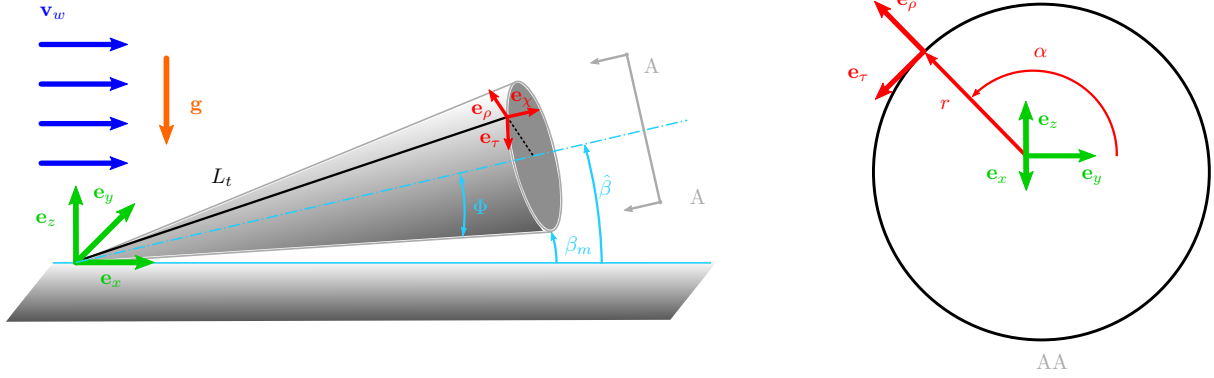
Figure 5. Cylindrical reference system $\mathcal{F}_C$ used to analyze circular trajectories.

5.1   Optimizing for the Mean Electrical Power in absence of Gravity

For the most idealized case, the gravity is null $g = 0$, such that $F_r \to \infty$ and $G_r = 0$. The objective function is taken as the mean electrical power, given in Eq. 15. By solving the OCP for the example (Table 1), it is found that the solution has constant values over the trajectory and the average power output is equal to the one evaluated with the analytical expression in Eq. 29. Figure 6 shows the evolution of β and ϕ, highlighting that the solution is a circle. Due to the constant values of the solution, quantities such as tether force along the axial symmetry axis, γ, AWES velocity and others can be found with the formulation assuming a crosswind straight motion, as Sect. 3.
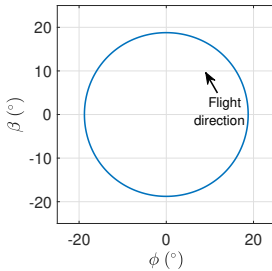
Figure 6. Optimal trajectory.

For the solution to be optimal, it is found that the AWES span is perpendicular to the wind speed, or, in analytical terms, that $\psi = 0$. Figure 7 shows the optimal opening angle Φ^* as a function of a modified non-dimensional mass parameter M_t found by solving a number of OCPs with different G ($G \in [10\ 30]$), M ($M \in [0.025\ 0.15]$) and $C_D \frac{A}{A_t}$ ($C_D \frac{A}{A_t} \in [0\ 0.4]$).

The values of Φ^* can be accurately described by

$$\tilde{\Phi} = \arccos\left(-\frac{M_t}{2} + \frac{\sqrt{M_t^2 + 4}}{2}\right), \qquad M_t = \frac{M}{1 + \frac{1}{G_t^2}},$$

(36)

which for high glide ratios coincides with the analytical formulation given in Trevisi et al. (2020a).
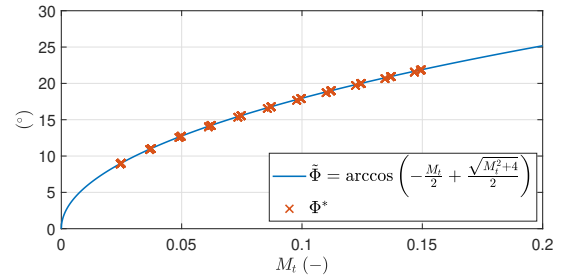
Figure 7. Optimal opening angles Φ^* (x) found by solving multiple OCPs and analytical expression (-) as a function of the modified non-dimensional mass parameter M_t.

5.2   Optimizing for the Mean Thrust Power considering Gravity

Gravity is now included in the modelling and the objective function is taken as the mean thrust power $\hat{P}_t$ (Eq. 12). The results of two slightly different OCPs are shown for the sake of understanding the results and they are summarized in Table 2. In OCP A, the control inputs are modelled with 5 harmonics. In OCP B, the time series of the control input ψ is modelled as a constant and only one harmonic is used for the control input γ. Additionally, the norm of the AWES velocity $v = |\mathbf{v}|$ is imposed to be constant (additional equality constraint). As the control inputs act up to the first harmonic, this constraint is set by imposing the first Fourier coefficients of the AWES velocity to zero ($\mathbf{R} = [V_{1,s}; V_{1,c}]$), while no constraints are imposed on the higher-order harmonics. In Table 2, the mean thrust power (objective function) is also reported and compared with the analytical formulation (Eq. 27). The objective function of the two OCPs is almost the same, showing that the two problems are basically equivalent.

Table 2. Settings of the two optimal control problems maximizing the mean thrust power considering gravity. $V_{1,s}$ and $V_{1,c}$ are the first Fourier coefficients of the norm of the AWES velocity v.

OCP	N_x	N_γ	N_ψ	size $\mathcal{X}$	$\mathbf{R}$	size $\mathbf{h}$	$\hat{P}_t$ (kW)	$\mathcal{T}$ (s)
A	10	5	5	65	-	42	285.4	12.8
B	10	1	0	47	$[V_{1,s}; V_{1,c}]$	44	284.5	12.7
L				analytical model			280.4	12.8

By solving the OCPs, it is found that the optimal solutions have a negative mean elevation of $\hat{\beta}_A \approx -8.2\,°$ and $\hat{\beta}_B \approx -7.8\,°$. The trajectories, shown in Figure 8, have a circular shape (a circle with radius $\tilde{\Phi}$ is marked as $-.$), but it is not any more a perfect circle.
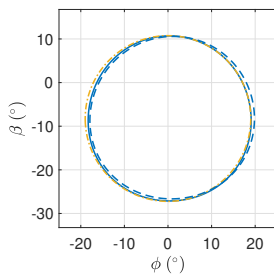
Figure 8. Optimal trajectory for OCP A (-), B (- -) and a circle with radius $\tilde{\Phi}$ ($-.$).

Figure 9 shows the trends of the control input ψ as a function of α (see Figure 5 for definition). For OCP A, it fluctuates with small amplitude about the mean value, which is close to zero. For this reason, it is modelled as a constant in OCP B. The optimal constant value is also close to zero, meaning that the AWES span is perpendicular to the wind speed direction. Since the two OCPs present similar optimal values of power, it is found that the optimal solutions are not sensitive to the fluctuations of the roll angle ψ.
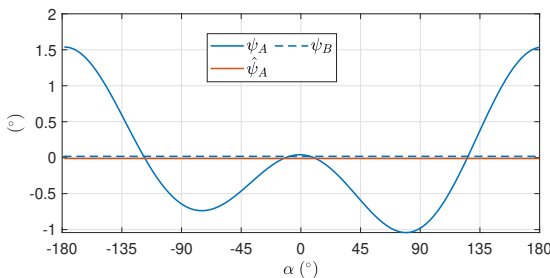
Figure 9. Optimal ψ as a function of the angular position.

Figure 10 shows the evolution of γ as a function of α. The mean values for the two OCPs are close to the value maximizing Eq. 27, denoted in figure as γ_L. γ takes values higher than the mean in the descending leg of the loop and negative

values in the ascendant leg. This means that in the ascendant leg the on-board wind turbines are operated as propellers. In OCP A γ is modelled with 5 harmonics, while in OCP B with just one. As the objective function of the two optimal solutions is similar, it is found that the trend of γ can be modelled with just one harmonic.
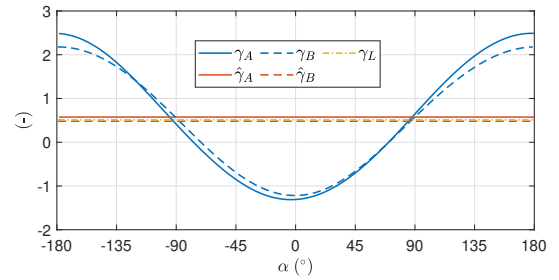
Figure 10. Optimal γ as a function of the angular position.

Figure 11 shows the norm of the optimal AWES velocity v for the two OCPs. In OCP B, this value is constrained to be a constant by imposing null only its first harmonic. Since it is not possible to impose constraints at frequencies where the control (γ and ψ) is not acting, higher-order harmonics are not constrained. The mean values of v are similar the one predicted by the steady model. Since the fluctuations for OCP A are small compared to the mean, the influence of the velocity fluctuations on the overall performances is investigated in OCP B, showing that they impact weakly the optimal solution. As the two OCPs problems are basically equivalent, it is found that optimal trajectories are characterized by a AWES constant velocity.

Figure 12 shows the magnitude of the tether force for the two cases. As it scales with the relative wind speed squared, also the tether force has an almost constant trend (the fluctuations are small compared to the mean).

To compare the two OCPs and draw some conclusions, the power output, shown in Figure 13, is to be analyzed. The mean thrust power output for the two OCPs is slightly higher than $P_{t,L}$. This is due to a non linear effect induced by the combination of gravity and mean elevation angle different from zero as compared to the idealized case. Indeed, for negative mean elevation, the combination leads to an increase of mean thrust power, while the opposite occurs in case of positive mean elevation. As the effects on power is
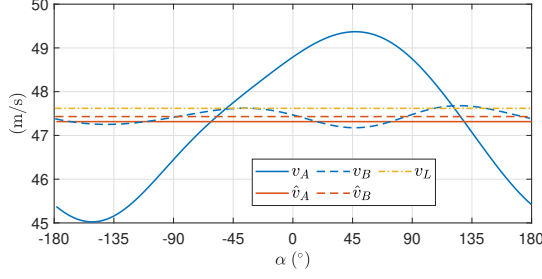
Figure 11. Norm of the optimal AWES velocity v as a function of the angular position.
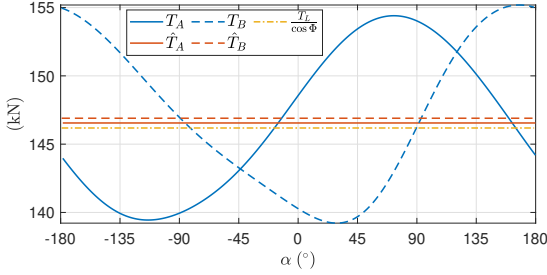
Figure 12. Tether force T as a function of the angular position.

almost negligible and it does not primarily impact the main outcomes of this paper, a detailed explanation of this phenomenon is here avoided, but the reader can find more details in Pasquinelli (2021). The theoretical thrust power, given in Eq. 27, is derived neglecting gravity. However, it approximates well the power output obtained through the OCP, which includes gravity.

As the two analyzed OCPs are almost equivalent, the optimal trajectories are characterized by the perpendicularity of the AWES span with respect to the wind ($\psi = 0$) and a constant AWES velocity. In order to keep the AWES velocity constant over the loop, the on-board wind turbines balance the action of the gravitational force. In the descendent leg, the on-board wind turbines harvest the gravitational potential energy and in the ascendant leg, that power is given back to the system.

Following these considerations, the power trend, as shown in Figure 13, can then be approximated as

$$P_t(\alpha) \approx P_{t,L} + \mathbf{F}_g \cdot \mathbf{v} \approx P_{t,L} - mgv_wG_t\cos\alpha. \qquad (37)$$

The on-board wind turbines thrust can be approximated with $\mathbf{D}_t \approx (\hat{\gamma} + A_{\gamma,1}\cos(\alpha - \theta_{\gamma,1}))\,\mathbf{D}$, where $\mathbf{D}$ is constant because the AWES velocity is found to be constant and from Fig. 10 it is found that $\theta_{\gamma,1} \approx 180°$. As the thrust power can be written as the product of $\mathbf{D}_t$ and the relative wind speed $\mathbf{v}_r$ (Eq. 12), the amplitude of the first Fourier coefficient of
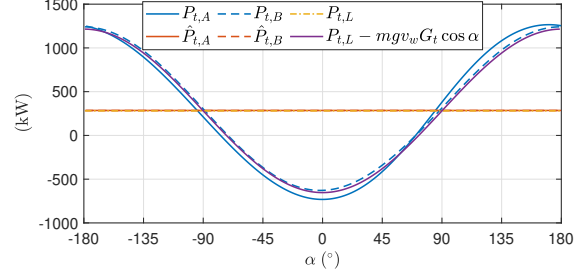
Figure 13. Optimal thrust power production and consumption P_t as a function of the angular position.

γ, considering Eq. 37, can be approximated by

$$A_{\gamma,1} \approx \frac{\mathbf{F}_g \cdot \mathbf{v}}{-\cos\alpha\,\mathbf{D} \cdot \mathbf{v}_r} \approx \frac{mg}{\frac{1}{2}\rho AC_D v_w^2 G_t^2} = G_rG. \qquad (38)$$

Figure 14 shows the comparison of $A_{\gamma,1}$ found numerically by running the OCP (with the settings of OCP B) for different combination of M ($M \in [0.025\ 0.15]$), G ($G \in [10\ 30]$) and F_r ($F_r \in [0.1\ 0.2]$) and the analytical approximation given in Eq. 38.
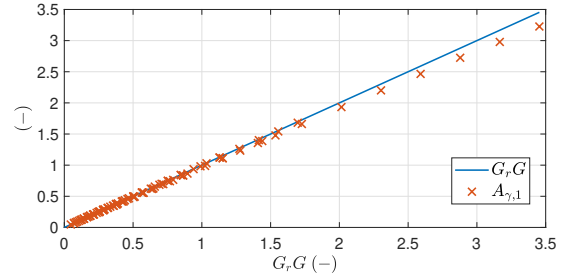
Figure 14. Amplitude of the first Fourier coefficient of γ (x) found by solving multiple OCPs and analytical approximation (-) as a function of G_rG.

Figure 15 shows the first Fourier coefficient of elevation β and azimuth ϕ as a function of the non-dimensional parameter M_t, as they represent the width and height of the trajectory. The analytical expression given in Eq. 36 is still a good approximation of the optimal trajectory shape.

5.3 Optimizing for the Mean Shaft Power considering Gravity

In this section, the on-board wind turbine induction is included in the power evaluation and the mean shaft power $\hat{P}_s$ is considered as objective function. To present the results, two different OCPs are introduced (Table 3). The mean shaft power for OCP A and B is almost identical, highlighting that one harmonic to model the productive drag and two for the roll are enough. The power for the analytical case is found by maximizing Eq. 28 with respect to γ. The figures in this section refer to OCP B.
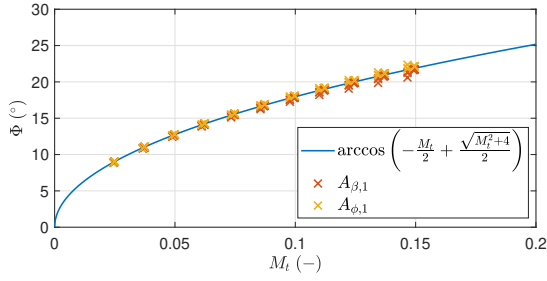
Figure 15. First Fourier coefficient of elevation β and azimuth ϕ (x) found by solving multiple OCPs and analytical expression (-) as a function of the modified non-dimensional mass parameter M_t.

Table 3. Settings of the two optimal control problems maximizing the mean shaft power considering gravity.

OCP	N_x	N_γ	N_ψ	size $\mathcal{X}$	size $\mathbf{h}$	$\hat{P}_s$ (kW)	$\mathcal{T}$ (s)
A	10	5	5	65	42	248.6	11.8
B	10	1	2	51	42	248.5	11.8
L		analytical model				272.5	12.6

Figure 16 shows the trajectory in the $\beta - \phi$ plane. The trajectory deviates from a circular shape, especially along the β axis, and has a mean elevation angle of $\hat{\beta}_B = -5.5°$, higher than for the case without induction.
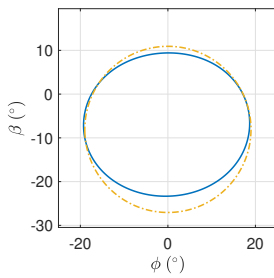
Figure 16. Optimal trajectory $(-)$ and a circle with radius $\tilde{\Phi}$.

5   Figure 17 shows the roll angle as a function of the angular position in the loop. Even in this case with induction, the fluctuations are relatively small. When the AWES increases the turning radius (approximately between $-90° < \alpha < 0°$ and $90° < \alpha < -180°$ (see Fig. 16), the roll decreases.
10   Figure 18 shows γ as a function of the angular position. The mean value is smaller compared to the value maximizing Eq. 28. By comparing the trends with Figure 10, it is clear that the fluctuations of γ are lower than in the case without induction. The on-board wind turbine induction has a similar
15   trend to γ, as they are linked through the expression in Eq. 28. When γ takes negative values -in the ascendant leg- the on-board wind turbines are operated as propellers and the induction is negative. In the descendant leg, γ takes values larger
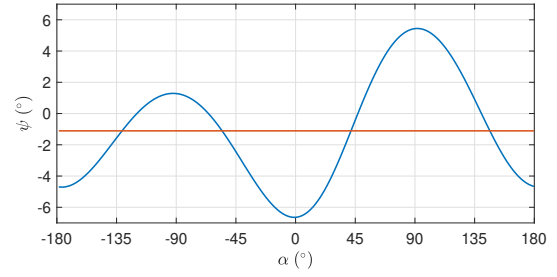
Figure 17. Optimal ψ (blue line) and its mean (red line) as a function of the angular position.

than the mean and so does the induction. Higher values of induction result in a lower ratio between shaft power, which is   20 the power the optimizer maximizes, and thrust power, which is the power directly linked to the dynamics. Therefore, high values of γ are not beneficial for the shaft power production.
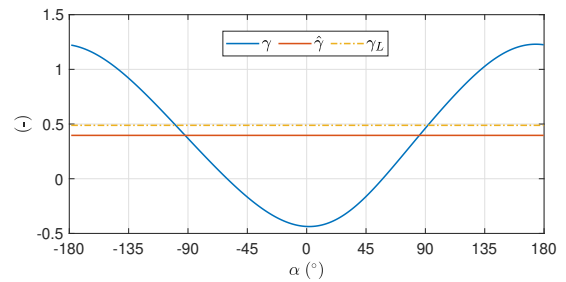
Figure 18. Optimal γ as a function of the angular position.

In Figure 19, the AWES velocity is shown, highlighting that it fluctuates over the loop. When maximizing the mean   25 thrust power (Sect. 5.2), the optimal AWES velocity over the loop was found to be constant. Here, it is optimal to convert part of the potential energy into electrical and part into kinetic energy, letting the velocity fluctuate over the loop.
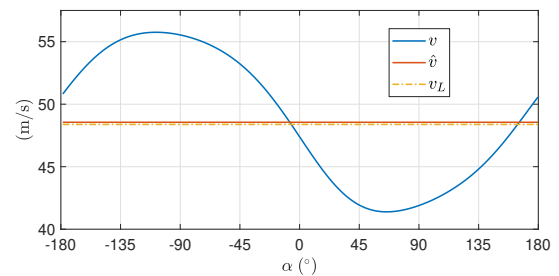
Figure 19. Norm of the optimal AWES velocity v as a function of the angular position.

To conclude the analysis of the example, Figure 20 shows   30 the shaft and the thrust power. As anticipated, when γ takes

higher values than the mean, the induction grows and the ratio between shaft and thrust power decreases consequently.
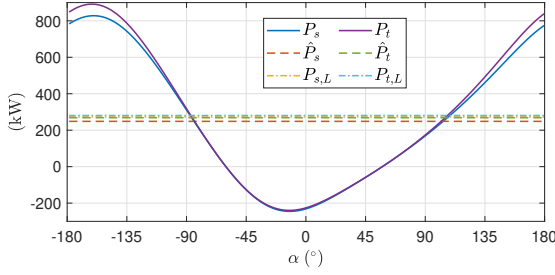
Figure 20. Optimal shaft power production and consumption P_s and thrust power P_t as a function of the angular position.

In Figure 4 the dependence of the analytical expression of the shaft power on $C_D \frac{A}{A_t}$ is shown. In Figure 21, the dependence of the optimal mean shaft power is analyzed as a function of the same non-dimensional coefficient for three different Froude numbers (i.e. three wind speeds). In the current example, $F_r = 0.1$ corresponds to $v_w = 5.4$ m s^{-1}, $F_r = 0.15$ corresponds to $v_w = 8.1$ m s^{-1} and $F_r = 0.2$ corresponds to $v_w = 10.8$ m s^{-1}. For increasing Froude number, the solution gets closer to the analytical formulation because the power fluctuations gradually lose impact on the mean power production. Indeed, the aerodynamic forces become dominant with respect to the gravitational force.
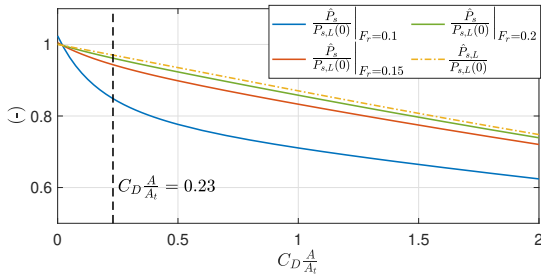
Figure 21. Optimal shaft power production normalized with the analytical expression of thrust power as a function of $C_D \frac{A}{A_t}$.

In Sect. 5.2, it was found that the amplitude of the first Fourier coefficient of γ for $C_D \frac{A}{A_t} = 0$ (i.e., optimizing for the thrust power) can be approximated by $A_{\gamma,1} \approx G_r G$. In Figure 22, the trends of $\frac{A_{\gamma,1}}{G_r G}$, being γ modeled with a single harmonic, for the three investigated Froude numbers, are shown as a function of $C_D \frac{A}{A_t}$. For $C_D \frac{A}{A_t} \to 0$, trends are close to 1. For increasing F_r, the curves collapse to a unique curve. In particular, at $C_D \frac{A}{A_t} = 0.23$, which is the value for the example, the ratio $\frac{A_{\gamma,1}}{G_r G} \to 0.54$ for increasing F_r. For increasing values of $C_D \frac{A}{A_t}$, the ratio $\frac{A_{\gamma,1}}{G_r G}$ tends to zero, highlighting the fact that a less fluctuating value of γ over the loop is beneficial. The plot shows also the value of $\hat{\gamma}$ as a function

of $C_D \frac{A}{A_t}$, highlighting that for increasing F_r the trends collapse to the value maximizing Eq. 28, indicated as γ_L.
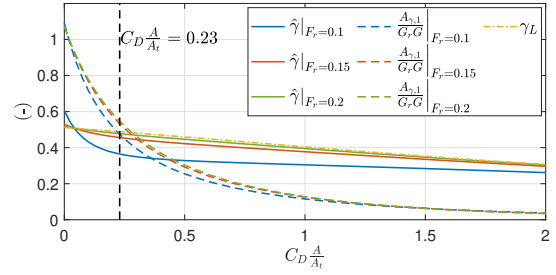
Figure 22. Optimal values of $\hat{\gamma}$ and $A_{\gamma,1}$, normalized with $G_r G$ as a function of $C_D \frac{A}{A_t}$ for different Froude numbers.

Finally, Figure 23 shows the ratio of the first Fourier coefficient of the elevation angle β and the azimuth angle ϕ with the opening angle $\tilde{\Phi}$ evaluated with Eq. 36. For $C_D \frac{A}{A_t} \to 0$, values are close to 1, as noted in Figure 15. As $C_D \frac{A}{A_t}$ increases, the values of $A_{\beta,1}$ decrease more than $A_{\phi,1}$, showing that optimal trajectory does not have any more a circular shape and the height decreases more than the width. This effect is visible also in the example, in Figure 16. At low Froude numbers (i.e. low wind speeds) this effect is more evident.
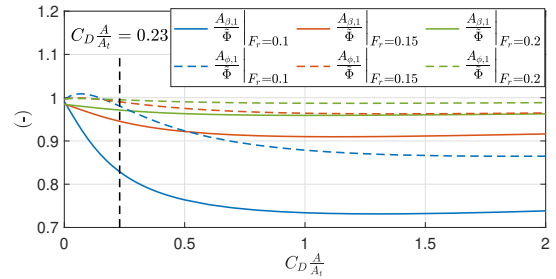
Figure 23. Optimal values of $A_{\beta,1}$ and $A_{\phi,1}$, normalized with the analytical expression of the opening angle $\tilde{\Phi}$, as a function of $C_D \frac{A}{A_t}$ for different Froude numbers.

5.4 Optimizing for the Mean Electrical Power considering Gravity

In this section, the electrical efficiency is included into the optimal control problem and the mean electrical power is considered as objective function. Two OCPs, whose characteristics are given in Table 4, are introduced to present results. The power for OCP A and B is almost identical, highlighting that one harmonic to model the productive drag and two for the roll are enough. The power for the analytical case is found by maximizing Eq. 29 with respect to γ.

Figure 24 shows the trajectory in the $\beta - \phi$ plane. The trajectories deviate from the circular trajectory with opening an-

Table 4. Settings of the two optimal control problems maximizing the mean electrical power considering gravity.

OCP	N_x	N_γ	N_ψ	size $\mathcal{X}$	size $\mathbf{h}$	$\hat{P}$ (kW)	$\mathcal{T}$ (s)
A	10	5	5	65	42	196.5	11.5
B	10	1	2	51	42	194.2	11.4
L		analytical model				218.0	12.6

gle $\tilde{\Phi}$ (Eq. 36), especially along the β axis, and have a mean elevation angle of $\hat{\beta}_A = -5.1°$ and $\hat{\beta}_B = -4.9°$.
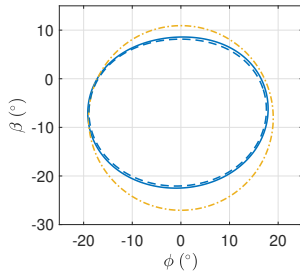
Figure 24. Optimal trajectory for OCP A (-), B (- -) and a circle with radius $\tilde{\Phi}$ (-.).

Figure 25 shows the roll angle as a function of the angular position in the loop. As in the case maximizing mean shaft power, the fluctuations are relatively small.
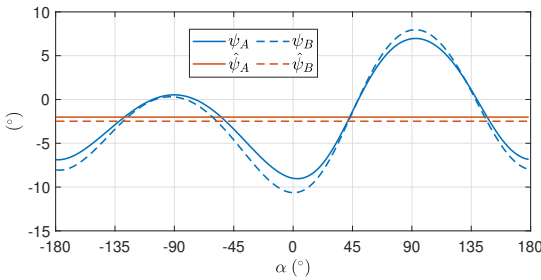
Figure 25. Optimal ψ as a function of the angular position.

Figure 26 shows γ as a function of the angular position. In OCP A, the time evolution of γ is modelled with 5 harmonics. In the ascendant leg, γ takes null values meaning that the power is neither spent neither consumed. Indeed, spending power drastically reduce the overall power production because of the conversion efficiency from electrical to thrust power. This is also highlighted by Tucker (2020). In OCP B, the time evolution of γ is modelled with just one harmonic. The trend is however similar to OCP A, with the minimum value being slightly negative. This means that $A_{\gamma,1}$ is similar to $\hat{\gamma}$.

Figure 27 shows the norm of the AWES velocity over the loop, showing that the trend is similar for the two OCPs and,
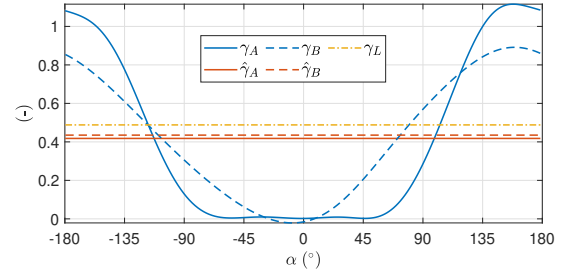
Figure 26. Optimal γ as a function of the angular position.

as noted in Sect. 5.3, it is optimal to convert part of the potential energy into electrical and part into kinetic energy.
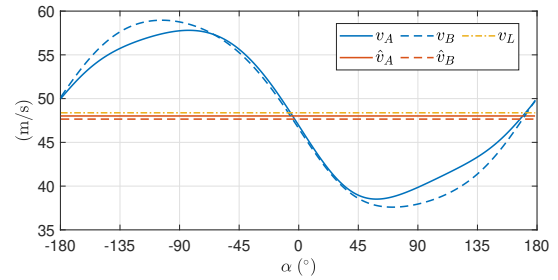
Figure 27. Norm of the optimal AWES velocity v as a function of the angular position.

The electrical power as a function of the angular position is shown in Figure 28. As expected when analyzing the trend of γ, the electrical power is null in the ascendant leg and larger than the mean in the descending part. In OCP B, the mean power is slightly lower than in OCP A but the power fluctuations are lower, which could be beneficial from a grid and power smoothing perspective. Due to the electrical efficiency, the wind turbines are not used as propellers anymore. This results in an even more squashed trajectory (Figure 24) with respect to the previous Sect. 5.3 (Figure 16) to partially limit the potential energy exchange into kinetic and so the AWES speed fluctuation.
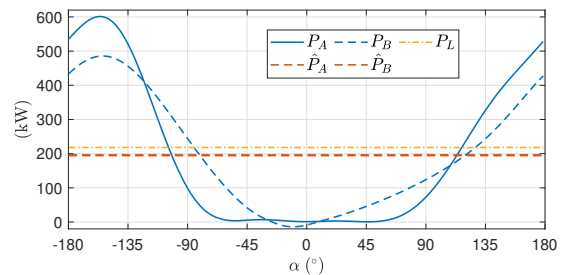
Figure 28. Optimal electrical power production as a function of the angular position.

One could try to investigate how the optimal values evolve for an increasing wind speed. Figure 29 shows the mean value of γ and its first Fourier coefficient $A_{\gamma,1}$ as a function of $G_r G$ (see Eq. 35 for definition) for OCP B. As noted when analyzing Figure 26, at $v_w = 6 \text{ m s}^{-1}$ $A_{\gamma,1}$ is slightly larger than $\hat{\gamma}$. As wind speed increases up to approximately 8.5 m s^{-1}, $A_{\gamma,1}$ keeps being similar to $\hat{\gamma}$, meaning that the minimum value of γ is close to zero and so is power ($P_{min} \approx 0$). If the wind speed increases again, $A_{\gamma,1}$ gets lower than $\hat{\gamma}$, meaning that power is always generated over the loop ($P_{min} > 0$). The main effect of the electrical efficiency on the OCP is to prevent the on-board wind turbines to be operated as propellers. Therefore, when the value of $A_{\gamma,1}$ which maximizes the shaft power P_s is larger than $\hat{\gamma}$, results are expected to be modified with respect to Sect. 5.3. Instead, when $A_{\gamma,1}$ is lower than $\hat{\gamma}$ trends are expected to be equal to the analyses in Sect. 5.3. Indeed, when analyzing Figure 22, it is found that $\frac{A_{\gamma,1}}{G_r G} \rightarrow 0.54$ for high F_r. This means that for low $G_r G$, the first Fourier coefficient of γ can be approximated with $A_{\gamma,1} \approx 0.54 \, G_r G$, as shown in Figure 29.
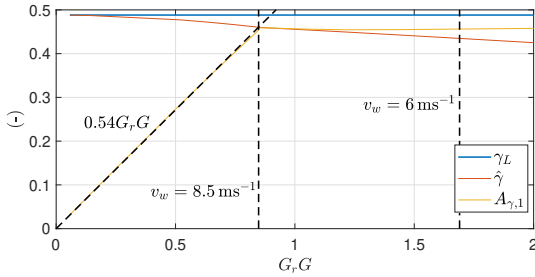
Figure 29. Optimal values of $\hat{\gamma}$ and $A_{\gamma,1}$ as a function of $G_r G$.

In Figure 30, the mean power normalized with the power evaluated with Eq. 29 is shown as a function of $G_r G$ for a case with $\eta_{el} = 1$, which is equivalent to the case in Sect. 5.3, and for a case with $\eta_{el} = 0.8$, as in this section. The two curves for wind speed lower than 8.5 m s^{-1} diverges. A low electrical efficiency η_{el} not only decreases the power output as in Eq. 29, but also decreases the efficiency with respect to the analytical approximation due to its effect on the dynamics.

To conclude, Figure 31 shows the evolution of the first Fourier coefficient of the elevation angle $A_{\beta,1}$ and of the azimuth $A_{\phi,1}$ as a function of $G_r G$. For high wind speed (i.e. low $G_r G$), their value is similar to the approximation given in Eq. 36. As $G_r G$ increases, for $\eta_{el} = 1$, $A_{\phi,1}$ stays almost constant while $A_{\beta,1}$ decreases. Smaller $A_{\beta,1}$ means smaller vertical height, which results in lower potential energy converted into electrical and kinetic energy over the loop. For $\eta_{el} = 0.8$ after $v_w = 8.5 \text{ m s}^{-1}$, both Fourier coefficients decrease rapidly meaning that smaller loops are performed. Smaller loops are therefore beneficial at low wind speed as they decrease the energy fluctuations.
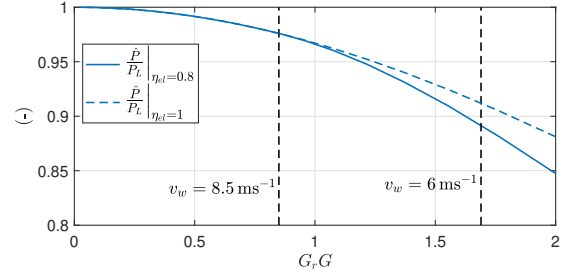
Figure 30. Normalized electrical power for a case with $\eta_{el} = 0.8$ (-) and $\eta_{el} = 1$ (- -) as a function of $G_r G$.
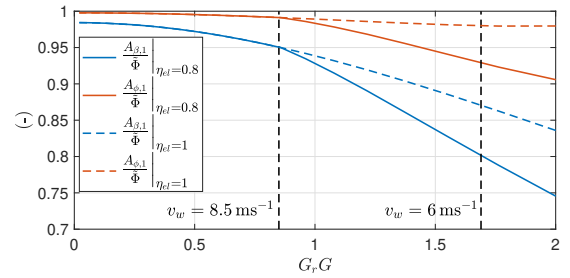
Figure 31. Optimal values of $A_{\beta,1}$ and $A_{\phi,1}$ normalized with the analytical expression of the opening angle $\tilde{\Phi}$ for a case with $\eta_{el} = 0.8$ (-) and $\eta_{el} = 1$ (- -) as a function of $G_r G$.

6 Optimal Control Problem considering Gravity, Wind Shear and Elevation Constraint

In this section, the wind shear is included in the problem. The reference altitude is taken $h_0 = 100$ m, the wind shear exponent $\alpha_s = 0.2$ and the reference wind speed $v_{w,0} = 6$ m s^{-1}. To make the problem more realistic, a constraint on the minimum elevation angle of $\beta_m = 10°$ (which is equivalent to a constraint on the minimum flight altitude) is included. The value of β_s needed to compute $\mathbf{e}_3$ and then the spanwise unit vector $\mathbf{s}$ (Eq. 5) is taken as the mean elevation angle $\beta_s = \hat{\beta}$. With this definition, the case of no roll ($\psi = 0$) is obtained when the wing span is in the plane perpendicular to the mean elevation angle, as in Trevisi et al. (2021).

Two OCPs are solved and they are summarized in Table 5. OCP A features 5 harmonics to model the control inputs, while OCP B has one harmonic to model the on-board wind turbine thrust and two for the roll, as in the previous sections. The two optimizations have similar mean electric power outputs, meaning that they are almost equivalent.

Figure 32 shows the trajectory for OCP A and B and compare it with a circle of radius $\tilde{\Phi}$ centered at an elevation of $\hat{\beta} = \arctan \sqrt{\alpha_s}$, as this formulation identifies the elevation of the center of the wind power window (Argatov et al. (2011)). As for the cases analyzed in Sect. 5.3 and 5.4, the trajectory is squashed along the vertical direction. The con-

Table 5. Settings of the two optimal control problems maximizing the mean power considering gravity and wind shear.

Case	N_x	N_γ	N_ψ	size $\mathcal{X}$	size $\mathbf{h}$	$\hat{P}$ (kW)	$\mathcal{T}$ (s)
A	10	5	5	65	42	115.3	11.5
B	10	1	2	51	42	113.3	11.4
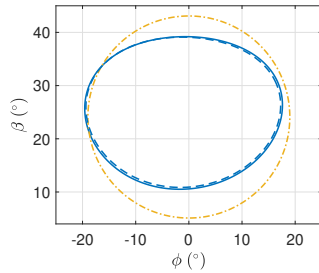
Figure 32. Optimal trajectory for case A (-), B (- -) and a circle with radius Φ (-.).

straint on the minimum elevation angle is not used, as the trajectory of both cases is always strictly higher than $\beta_m = 10°$.

The roll angle ψ is shown in Figure 33. In *LT-GliDe* (Trevisi et al. (2021)) the flight stability of AWES is studied by linearizing the equations of motion with respect to a fictitious steady state condition, where the AWES moves in a circular trajectory with a constant velocity. This steady state is characterized by the AWES span being perpendicular to the mean elevation angle direction. In this section, this condition is identified by $\psi = 0$. The roll fluctuations, shown in Figure 33, are limited in amplitude and might be considered within the linear bounds of the linearization validity of *LT-GliDe*. More analyses to prove this will be carried out in future works.

Figure 34 shows the evolution of the on-board wind turbines thrust coefficient as a function of the angular position for the two cases. The trends are similar to the analyses in Sect. 5.4. It is optimal to use the on-board wind turbines only to generate power and not as propellers. Even if the trends
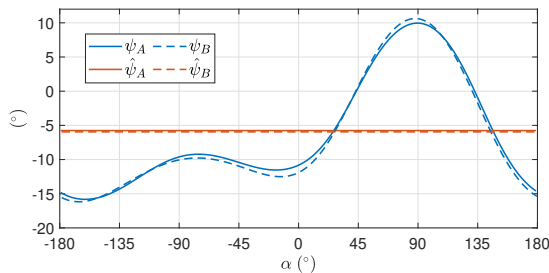
Figure 33. Optimal ψ as a function of the angular position.

of γ for OCP A and B are quite different, the overall power production is similar, meaning that power production is not sensitive to harmonics of γ higher than one.
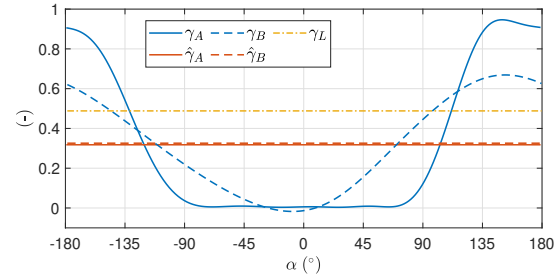
Figure 34. Optimal γ as a function of the angular position.

Figure 35 shows the wind speed that the AWES encounters over the loop due to the wind shear. Clearly, at the top of the loop ($\alpha = 90°$), the wind speed is the highest, sweeping approximately 1.5 m s^{-1} over the trajectory. In this section, the mean wind speed over the loop is used to evaluate the Froude number F_r (Eq. 34) and consequently the gravity ratio G_r (Eq. 35). These numbers will be used later in this section to generalize results.
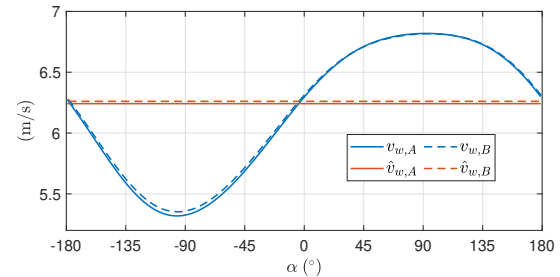
Figure 35. Wind velocity as a function of the angular position.

Figure 36 shows the AWES velocity as a function of the angular position. As discussed in the previous sections, in the descending leg the AWES convert the potential energy into electrical, producing power, and kinetic energy, accelerating. In the climbing leg instead electrical power is not spent and kinetic energy is transformed into potential.

Figure 37 shows the power production as a function of the angular position. When looking at power and tether force (not shown here as it follows the AWES velocity trend squared) to characterize the operations of a real system, the maximum power and the maximum and minimum tether force would be constrained not to exceed some given values. To properly include these constraints, additional control inputs, useful to model the de-powering of the AWES (e.g. the lift coefficient), shall be considered in the analysis.

As carried out in the previous section, trends are studied as a function of the Froude number for the optimal control problem B. Figure 38 shows the dependence of $\hat{\gamma}$ and $A_{\gamma,1}$
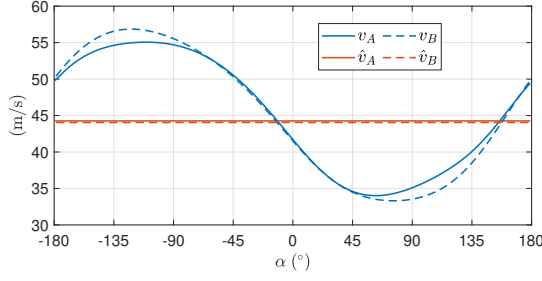
Figure 36. Norm of the optimal AWES velocity v as function of the angular position.
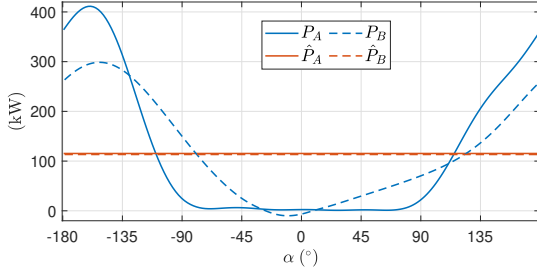
Figure 37. Optimal power production P as function of the angular position.

as a function of $G_r G$. $\hat{\gamma}$ decreases when $G_r G$ increases (i.e., the wind speed decreases). At low wind speed, $\hat{\gamma}$ takes low values so that the AWES speed over the loop is higher, which is beneficial to stay airborne. $A_{\gamma,1}$ for low $G_r G$ has a linear
5 trend, as noted in Sect. 5.4. When $A_{\gamma,1}$ is equal to $\hat{\gamma}$, the minimum power production over the loop is null. For lower wind speeds (i.e., higher $G_r G$), it is not optimal anymore to increase $A_{\gamma,1}$ because the on-board wind turbines would be used as propellers with a high penalty on the mean power
10 production.
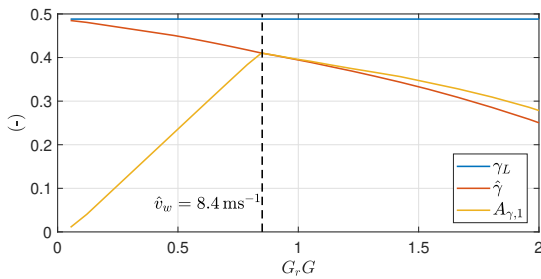
Figure 38. Optimal values of $\hat{\gamma}$ and $A_{\gamma,1}$ as a function of $G_r G$.

To conclude, Figure 39 shows the ratio of the first Fourier coefficient of β and ϕ with respect to the analytical expression of the opening angle $\tilde{\Phi}$ for a case maximizing electrical power ($\eta_{el} = 0.8$) and shaft power ($\eta_{el} = 1$). After the cusp
15 in Figure 38, the two trends diverge and for $\eta_{el} = 0.8$ smaller

loops are optimal so that the exchange of potential energy over the loop is reduced.
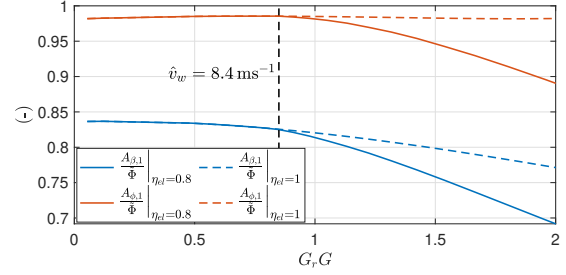
Figure 39. Optimal values of $A_{\beta,1}$ and $A_{\phi,1}$ normalized with the analytical expression of the opening angle $\tilde{\Phi}$ for a case with $\eta_{el} = 0.8$ (-) and $\eta_{el} = 1$ (- -) as a function of $G_r G$.

7   Conclusions and Discussion

In this work, a novel methodology to study optimal trajectories for Fly-Gen AWES is introduced. The chosen low-
20 fidelity dynamic model is characterized by two degrees of freedom (the AWES is modelled as a point mass with constant tether length) and two control inputs. The degrees of freedom are the elevation and the azimuth angle. The control inputs are the roll angle, defined as the rotation around
25 the relative velocity direction, and the on-board wind turbines thrust coefficient. An Optimal Control Problem is formulated in the frequency domain through a Harmonic Balance method. Working with the Fourier coefficients of the time series, instead of the time series themselves, allows to
30 potentially reduce the problem size, to implicitly impose periodicity and to gain an intuitive understanding of the results by analyzing the harmonic contributions. Moreover, the analytical gradient of the objective function and the constraints with respect to the optimization variables can be provided to
35 the solver, allowing for a deep and fast convergence of the optimal solutions.

The *MX2* design from Tucker (2020) is taken as a reference AWES to introduce the results. To isolate the effects of each physical phenomenon, results are presented with an
40 increasing level of complexity from the most idealized case and they are compared with analytical solutions from literature, whenever possible. A set of idealized case studies with no constraint on the minimum elevation angle and uniform wind inflow are initially studied. If gravity is neglected, the
45 solution is steady and it can be described by analytical expressions. If gravity is considered, three different optimal control problems, characterized by three different objective functions, are solved:

i) If the mean thrust power (mechanical power neglecting
50 on-board wind turbines induction) is the objective function, the optimal trajectories are circular, have a constant AWES velocity and the wing span is perpendicular to the incom-

ing wind. To obtain this condition, all the potential energy is converted into electrical by the on-board wind turbines. At low wind speed, on-board wind turbines are then used as propellers in the ascendant part of the loop. The optimal power, the trajectory shape and the production strategy can be accurately approximated with analytical expressions;

ii) If the mean shaft power (mechanical power considering on-board wind turbines induction) is the objective function, the potential energy, in the descending leg, is partially converted into electrical and partially into kinetic energy. This is because the power conversion penalizes solutions with high on-board wind turbines induction. Therefore, the velocity fluctuates over the loop and the trajectories are squashed along the vertical direction to decrease the potential energy exchange;

iii) If the mean power electrical provided to the grid is the objective function (i.e. the electrical efficiency is included), the on-board wind turbines never operate as propellers. If operated as propellers, power would be converted from mechanical into electrical while descending and from electrical into mechanical while ascending, leading to large power losses due to the electrical efficiency. This effect is found only at low wind speed, when propelling the AWES in the climbing leg maximizes the mean shaft power. Past a given wind speed, using the on-board wind turbines as propellers does not maximize the mean shaft power and the influence of the electrical efficiency on the production strategy vanishes.

When the wind shear and a constraint on the minimum elevation angle are included in the optimal control problem for maximizing the electrical power, trends are similar to the case with uniform inflow. Therefore, the power production strategy does not heavily depend on the wind shear. For the analyzed example, the constraint on the minimum elevation angle is not active.

For all the analyzed cases, additional analytical approximations characterizing the solution are introduced. These approximations are found by modelling the control inputs with the lowest number of harmonics. The on-board wind turbines thrust can be modelled with just one harmonic and the roll with two harmonics without loss of generality of the results.

The results of this work align with the discussions in Tucker (2020) and have a strong mathematical foundation, as the trajectory and the control inputs are found by solving optimal control problems. These methods are planned to be applied, with appropriate modifications, to other AWE architectures and to other trajectory types. A comparison between circular and figure of eight trajectories is foreseen. Finally, the physical understanding and methods proposed here are envisaged to be incorporated into the design, analysis and optimization framework *T-Glide* (Trevisi et al. (2022)), with the aim of improving the power estimation and including an optimal control module.

Nomenclature

Latin Symbols

A	Wing area	55
$A_{\beta,1}$	Amplitude of the first Fourier harmonic of β	
$A_{\gamma,1}$	Amplitude of the first Fourier harmonic of γ	
$A_{\phi,1}$	Amplitude of the first Fourier harmonic of ϕ	
A_t	Total on-board wind turbines area	
a	On-board wind turbines induction	60
C_D	Drag coefficient	
C_L	Lift coefficient	
$\mathbf{F}_g$	Gravitaional force	
F_r	Froude number	
G	System glide ratio	65
G_r	Gravity ratio	
G_t	Modified system glide ratio	
$\mathbf{g}$	Inequality constraints	
g	Gravitational acceleration	
$\mathbf{h}$	Equality constraints	70
L_t	Tether length	
M	Non dimensional mass parameter	
M_t	Modified non dimensional mass parameter	
m	AWES mass	
N_γ	Order of the Fourier series of the control input γ	75
N_ψ	Order of the Fourier series of the control input ψ	
N_x	Order of the Fourier series of the state variables	
P	Electrical power	
P_s	Shaft power	
P_t	Thrust power	80
$\mathbf{R}$	Additional equality constraints in the frequency domain	
T	Norm of the tether force	
v_w	Norm of the wind velocity	
$\mathbf{v}$	AWES velocity	
v	Norm of the AWES velocity	85
$\mathbf{v}_r$	Relative wind speed	

Greek Symbols

α	Angular position in the loop	
β	Elevation angle	90
η_{el}	Electrical conversion efficiency	
γ	On-board wind turbines factor	
ω	Revolution frequency	
Φ	Opening angle of the trajectory	
ϕ	Azimuth angle	95
ψ	Roll angle	
ρ	Air density	
$\mathcal{T}$	Revolution period	
$\mathcal{X}$	Optimization variables	
		100

Symbols

$\hat{\cdot}$	Mean value	
$\cdot_L$	Quantity evaluated with the Steady State (Loyd) model	

Appendix A: Figures of Comparison between Frequency-Domain Formulation and Time Integration

Author contributions. FT, ICF, and GP conceptualized the study and the research methods. FT developed the research methods. FT and ICF developed the code. FT produced the results and wrote the draft version of the paper. CEDR and AC supervised the research. ICF, GP, CEDR and AC reviewed the draft version.

Competing interests. The authors declare that they have no conflict of interest.
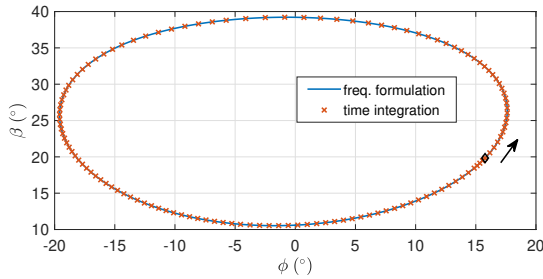
Figure A1. Azimuth and elevation of the trajectory found with the harmonic balance method and the time integration scheme for a circular shaped trajectory.
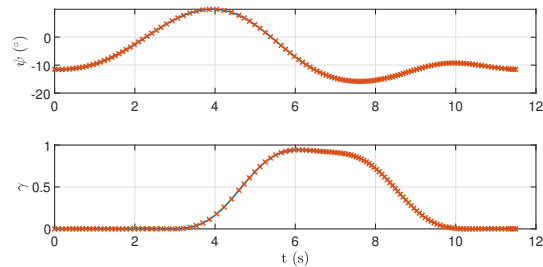
Figure A2. Time series of the control inputs provided to the harmonic balance method and the time integration scheme for a circular shaped trajectory.
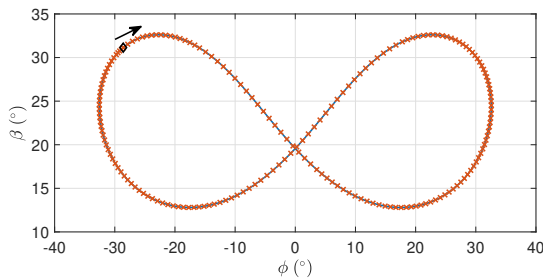
Figure A3. Azimuth and elevation of the trajectory found with the harmonic balance method and the time integration scheme for a figure of eight shaped trajectory.
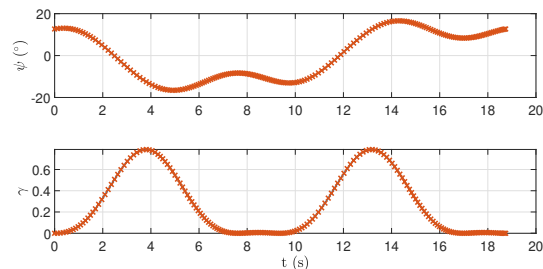
Figure A4. Time series of the control inputs provided to the harmonic balance method and the time integration scheme for a figure of eight shaped trajectory.

Acknowledgements. The work by ICF was carried out under the framework of the GreenKite-2 project (PID2019-110146RB-I00) funded by MCIN/AEI/10.13039/501100011033.

References

Argatov, I., Rautakorpi, P., and Silvennoinen, R.: Apparent wind load effects on the tether of a kite power generator, Journal of Wind Engineering and Industrial Aerodynamics, 99, 1079–1088, https://doi.org/10.1016/j.jweia.2011.07.010, 2011.

awebox: Modelling and optimal control of single- and multiple-kite systems for airborne wind energy, https://github.com/awebox/awebox, 2022.

Cobb, M. K., Barton, K., Fathy, H., and Vermillion, C.: Iterative Learning-Based Path Optimization for Repetitive Path Planning, With Application to 3-D Crosswind Flight of Airborne Wind Energy Systems, IEEE Transactions on Control Systems Technology, 28, 1447–1459, https://doi.org/10.1109/TCST.2019.2912345, 2020.

De Schutter, J., Leuthold, R., Bronnenmeyer, T., Paelinck, R., and Diehl, M.: Optimal control of stacked multi-kite systems for utility-scale airborne wind energy, in: 2019 IEEE 58th Conference on Decision and Control (CDC), pp. 4865–4870, https://doi.org/10.1109/CDC40024.2019.9030026, 2019.

Dimitriadis, G.: Time Integration, in: Introduction to Nonlinear Aeroelasticity, chap. 3, pp. 63–111, John Wiley & Sons, Ltd, https://doi.org/10.1002/9781118756478.ch3, 2017.

Eijkelhof, D. and Schmehl, R.: Six-Degrees-Of-Freedom Simulation Model for Future Multi-Megawatt Airborne Wind Energy Systems, SSRN Electronic Journal, https://doi.org/10.2139/ssrn.4003237, 2022.

Fagiano, L., Zgraggen, A. U., Morari, M., and Khammash, M.: Automatic Crosswind Flight of Tethered Wings for Airborne Wind Energy: Modeling, Control Design, and Experimental Results, IEEE Transactions on Control Systems Technology, 22, 1433–1447, https://doi.org/10.1109/TCST.2013.2279592, 2014.

Fechner, U. and Schmehl, R.: Flight path control of kite power systems in a turbulent wind environment, in: 2016 American Control Conference (ACC), pp. 4083–4088, https://doi.org/10.1109/ACC.2016.7525563, 2016.

Fechner, U., van der Vlugt, R., Schreuder, E., and Schmehl, R.: Dynamic model of a pumping kite power system, Renewable Energy, 83, 705–716, https://doi.org/10.1016/j.renene.2015.04.028, 2015.

Fernandes, M. C. R. M., Paiva, L. T., and Fontes, F. A. C. C.: Optimal Path and Path-Following Control in Airborne Wind Energy Systems, in: Advances in Evolutionary and Deterministic Methods for Design, Optimization and Control in Engineering and Sciences, edited by Gaspar-Cunha, A., Periaux, J., Giannakoglou, K. C., Gauger, N. R., Quagliarella, D., and Greiner, D., pp. 409–421, Springer International Publishing, Cham, https://doi.org/10.1007/978-3-030-57422-2_26, 2021.

Gros, S. and Diehl, M.: Modeling of Airborne Wind Energy Systems in Natural Coordinates, in: Airborne Wind Energy, edited by Ahrens, U., Diehl, M., and Schmehl, R., pp. 181–203, Green Energy and Technology. Springer, Singapore, https://doi.org/10.1007/978-3-642-39965-7_10, 2013.

Gros, S., Zanon, M., and Diehl, M.: A relaxation strategy for the optimization of Airborne Wind Energy systems, in:

2013 European Control Conference (ECC), pp. 1011–1016, https://doi.org/10.23919/ECC.2013.6669670, 2013.

Haas, T., De Schutter, J., Diehl, M., and Meyers, J.: Wake characteristics of pumping mode airborne wind energy systems, in: Journal of Physics: Conference Series, vol. 1256, p. 012016, IOP Publishing, https://doi.org/10.1088/1742-6596/1256/1/012016, 2019.

Horn, G., Gros, S., and Diehl, M.: Numerical trajectory optimization for airborne wind energy systems described by high fidelity aircraft models, in: Airborne Wind Energy, edited by Ahrens, U., Diehl, M., and Schmehl, R., pp. 205–218, Springer, https://doi.org/10.1007/978-3-642-39965-7_11, 2013.

Jonkman, J., Hayman, G., Mudafort, R., Damiani, R., Wendt, F., Google Incorporated, and USDOE: KiteFAST, https://www.osti.gov//servlets/purl/1786962, 2018.

Lau, S. L., Cheung, Y. K., and Wu, S. Y.: A variable parameter incrementation method for dynamic instability of linear and nonlinear elastic systems, J. Appl. Mech. Trans. ASME, 49, 849–853, https://doi.org/10.1115/1.3162626, 1982.

Leuthold, R., De Schutter, J., Malz, E. C., Licitra, G., Gros, S., and Diehl, M.: Operational Regions of a Multi-Kite AWE System, in: 2018 European Control Conference (ECC), pp. 52–57, https://doi.org/10.23919/ECC.2018.8550199, 2018.

Licitra, G., Koenemann, J., Bürger, A., Williams, P., Ruiterkamp, R., and Diehl, M.: Performance assessment of a rigid wing Airborne Wind Energy pumping system, Energy, 173, 569–585, https://doi.org/10.1016/j.energy.2019.02.064, 2019.

Loyd, M.: Crossswind Kite Power, Journal of Energy, 4, 106–111, 1980.

Malz, E., Koenemann, J., Sieberling, S., and Gros, S.: A reference model for airborne wind energy systems for optimization and control, Renewable Energy, 140, 1004–1011, https://doi.org/10.1016/j.renene.2019.03.111, 2019.

Malz, E., Hedenus, F., Göransson, L., Verendel, V., and Gros, S.: Drag-mode airborne wind energy vs. wind turbines: An analysis of power production, variability and geography, Energy, 193, 116 765, https://doi.org/10.1016/j.energy.2019.116765, 2020a.

Malz, E., Verendel, V., and Gros, S.: Computing the power profiles for an Airborne Wind Energy system based on large-scale wind data, Renewable Energy, 162, 766–778, https://doi.org/10.1016/j.renene.2020.06.056, 2020b.

Pasquinelli, G.: An Engineering Model for Power Generation Estimation of Crosswind Airborne Wind Energy Systems, Master's thesis, Politecnico di Milano, https://doi.org/10.13140/RG.2.2.31882.39363, 2021.

Pierre, C. and Dowell, E. H.: A Study of Dynamic Instability of Plates by an Extended Incremental Harmonic Balance Method, J. Appl. Mech., 52, 693–697, 1985.

Rapp, S., Schmehl, R., Oland, E., and Haas, T.: Cascaded Pumping Cycle Control for Rigid Wing Airborne Wind Energy Systems, Journal of Guidance, Control, and Dynamics, 42, 2456–2473, https://doi.org/10.2514/1.G004246, 2019.

Schelbergen, M. and Schmehl, R.: Validation of the quasisteady performance model for pumping airborne wind energy systems., Journal of Physics: Conference Series, 1618, https://doi.org/10.1088/1742-6596/1618/3/032003, 2020.

Stuyts, J., Horn, G., Vandermeulen, W., Driesen, J., and Diehl, M.: Effect of the Electrical Energy Conversion on Optimal Cycles for Pumping Airborne Wind En-

ergy, IEEE Transactions on Sustainable Energy, 6, 2–10, https://doi.org/10.1109/TSTE.2014.2349071, 2015.

Sánchez-Arriaga, G. and Serrano-Iglesias, J.: Modeling and Natural Mode Analysis of Tethered Multi-Aircraft Systems, Journal of Guidance, Control, and Dynamics, 44, 1199–1210, https://doi.org/https://doi.org/10.2514/1.G005075, 2021.

Sánchez-Arriaga, G., García-Villalba, M., and Schmehl, R.: Modeling and dynamics of a two-line kite, Applied Mathematical Modelling, 47, 473–486, https://doi.org/https://doi.org/10.1016/j.apm.2017.03.030, 2017.

Sánchez-Arriaga, G., Pastor-Rodríguez, A., Sanjurjo-Rivo, M., and Schmehl, R.: A lagrangian flight simulator for airborne wind energy systems, Applied Mathematical Modelling, 69, 665–684, https://doi.org/10.1016/j.apm.2018.12.016, 2019.

Todeschini, D., Fagiano, L., Micheli, C., and Cattano, A.: Control of a rigid wing pumping Airborne Wind Energy system in all operational phases, Control Engineering Practice, 111, 104 794, https://doi.org/https://doi.org/10.1016/j.conengprac.2021.104794, 2021.

Trevisi, F., Gaunaa, M., and Mcwilliam, M.: The Influence of Tether Sag on Airborne Wind Energy Generation., Journal of Physics: Conference Series, 1618, https://doi.org/10.1088/1742-6596/1618/3/032006, 2020a.

Trevisi, F., Gaunaa, M., and Mcwilliam, M.: Unified engineering models for the performance and cost of Ground-Gen and Fly-Gen crosswind Airborne Wind Energy Systems, Renewable Energy, 162, 893–907, https://doi.org/10.1016/j.renene.2020.07.129, 2020b.

Trevisi, F., Croce, A., and Riboldi, C. E. D.: Flight Stability of Rigid Wing Airborne Wind Energy Systems, Energies, 14, https://doi.org/10.3390/en14227704, 2021.

Trevisi, F., Riboldi, C. E. D., and Croce, A.: Sensitivity analysis of a Ground-Gen Airborne Wind Energy System design., Journal of Physics: Conference Series, 2265, 042 067, https://doi.org/10.1088/1742-6596/2265/4/042067, 2022.

Tucker, N.: Airborne Wind Turbine Performance: Key Lessons From More Than a Decade of Flying Kites., in: The Energy Kite Part I., edited by Echeverri, P., Fricke, T., Homsy, G., and Tucker, N., pp. 93–224, Makani Technologies LLC, 2020.

van der Vlugt, R., Bley, A., Noom, M., and Schmehl, R.: Quasisteady model of a pumping kite power system, Renewable Energy, 131, 83–99, https://doi.org/10.1016/j.renene.2018.07.023, 2019.

Vermillion, C., Cobb, M., Fagiano, L., Leuthold, R., Diehl, M., Smith, R. S., Wood, T. A., Rapp, S., Schmehl, R., Olinger, D., and Demetriou, M.: Electricity in the air: Insights from two decades of advanced control research and experimental flight testing of airborne wind energy systems, Annual Reviews in Control, 52, 330–357, https://doi.org/10.1016/j.arcontrol.2021.03.002, 2021.